

Long-term Lidar Observations of the Gravity Wave Activity near the Mesopause at Arecibo

Xianchang Yue^{1,2}, Jonathan S. Friedman⁴, Qihou Zhou⁵, Xiongbin Wu^{1,2}, Jens Lautenbach³

¹School of Electronic Information, Wuhan University, Wuhan, 430072, China

5 ²Collaborative Innovation Center of Geospatial Technology, 129 Luoyu Road, Wuhan, 430072, China

³Arecibo Observatory – University of Central Florida, Arecibo, Puerto Rico.

⁴Puerto Rico Photonics Institute, School of Science and Technology, Universidad Metropolitana, Cupey, Puerto Rico.

⁵Electrical and Computer Engineering Department, Miami University, Oxford, Ohio, USA

Correspondence to: Xianchang Yue (yuexc@whu.edu.cn)

10 **Abstract.** 11-years long K Doppler lidar observations of temperature profiles in the mesosphere and lower thermosphere
(MLT) between 85 and 100 km, conducted at the Arecibo Observatory, Puerto Rico (18.35°N, 66.75°W), are used to
estimate seasonal variations of the mean temperature, the squared Brunt-Väisälä frequency, N^2 , and the gravity wave
potential energy in a composite year. The following unique features are obtained: 1. The mean temperature structure shows
similar characteristics as a prior report based on a smaller dataset: 2. Temperature Inversion Layers (TILs) occur at ~96 km
15 in spring, at ~91 km in summer and early autumn, and at ~94 km in winter; 3. The first complete range-resolved climatology
of Gravity Wave Potential Energy (GWPE) derived from temperature data in the tropical MLT exhibits an altitude
dependent combination of annual oscillation (AO) and semiannual oscillation (SAO). The maximum occurs in spring and the
minimum in summer, a second maximum is in autumn and a second minimum in winter; 4. The GWPE per unit volume
damps below ~97 km altitude in all seasons. The damp of GWPE is significant at and below the TILs but becomes faint
20 above, this provides strong support to the mechanism that the formation of upper mesospheric TIL is due mainly to the damp
of GWPE. The climatology of GWPE shows an indeed pronounced altitudinal and temporal correlation with the wind field
in the equator mesopause region published in the literatures. This suggests the GW activity in the tropical mesopause region
should be manifested mainly by the filtering effect of critical level of the local background wind.

1 Introduction

25 Gravity Waves (GWs) are believed to be the primary force driving the large-scale circulation and coupling of different
atmospheric layers due to their momentum and energy deposition when breaking or dissipating (Fritts and Alexander, 2003;
Lindzen, 1981; Smith, 2012). Gravity waves often originate from copious tropospheric sources and propagate upward. Their
amplitudes grow rapidly with altitude under the condition of atmospheric density decreasing and begin to break or dissipate
in the MLT where gravity wave influences have been shown to be strong by various observations (e.g., Baumgarten et al.
30 2018; 2017; 2015; Cai et al., 2014; Gardner and Liu, 2010; Li et al., 2010; Lu et al., 2009; Yuan et al., 2016). Gravity waves

are therefore an essential component in current General Circulation Models (GCMs) [e.g., Liu and Meriwether, 2004; Picone et al., 2002]. Associated modeling studies have shown that including the effects of GWs is a key to simulate realistic quasi-biennial and semiannual oscillations and other phenomena in the stratosphere and mesosphere [e.g., Dunkerton, 1997; Huang et al. 2010; Xu et al., 2006].

5 The upward propagations of GWs are often influenced by the background wind fields (e.g., Yigit and Medvedev, 2017). The altitude ranges, where GWs interact with the background wind dissipating and depositing energy and momentum is of high interest to researchers. This happens mainly in the middle atmosphere near or between stratopause and mesopause. Above 35 km altitude, the semiannual oscillation (SAO) shows a predominance in the annual variability of the zonal winds (e.g., Garcia et al., 1997; Hirota, 1980). The SAO phase of zonal winds shifts approximately 180° with the altitude increasing from
10 stratosphere to mesosphere. The stratospheric SAO leads to a seasonal variation of filtering of the upward propagating waves, which results in a specific seasonal variation of GW activity in the mesosphere.

The mean zonal winds in mesosphere and lower thermosphere (MLT) have been measured by both ground-based radar (e.g., Garcia et al., 1997; Lieberman et al., 1993) and satellites such as the High-Resolution Doppler Imager (HRDI), Wind Imaging Interferometer (WINDII) and the Microwave Limb Sounder (MLS) on board the Upper Atmosphere Research
15 Satellite (UARS) or the Doppler Interferometer (TIDI) on board the Thermosphere Ionosphere Mesosphere Energetics and Dynamics (TIMED) satellite (e.g., Smith, 2012). They show different features of the zonal winds in the mesopause range from tropical region to middle latitude regions. Garcia et al. (1997) and Smith (2012) showed that, for example, the westerly wind prevailed in the range 80-95 km both in January and July in the HRDI equatorial zonal wind but it reversed below or
20 or higher in July at higher latitude in the north hemisphere. The monthly mean HRDI equatorial zonal wind showed that, the easterly winds were prevailing in equinoxes seasons near 80 km altitude. They then decreased with altitude from 80 km above and turned to increase above ~ 92 km, while the westerly winds prevailed in the range 80-94 km in solstice seasons, they then turn to be easterly. the reversal is at about 95 km (Smith, 2012). Therefore, the zonal winds are low or zero around
25 92 km altitude in tropical region. The zero-wind lines will enhance damping or dissipating of zonal propagating gravity wave with low to moderate phase speed.

Temperature is a crucial parameter indicating the state of the atmosphere. To measure the temperature in the MLT region, satellite and lidar techniques have been developed in recent decades. Satellite measurements have the advantage of resolving large spatial scale wave structures, but the short-term variability in dynamical features gets lost. While for the lidar measurements, they provide a vertical profile of temperature with a suitable temporal and vertical resolution at a particular
30 location. Lidar data can well resolve gravity waves with short and medium periods and their temporal development. The perturbation or standard deviation from zonal mean temperature is often used as a wave activity indicator in the atmosphere. For instance, Offermann et al. (2006) use the temperature measured from CRISTA (CRYogenic Infrared Spectrometers and Telescopes for the Atmosphere) and from SABER (Sounding of the Atmosphere using Broadband Emission Radiometry) to investigate the global wave activity from upper stratosphere to lower thermosphere. They showed quite different wave

behaviours below and above their defined ‘wave-turbopause’ close to but lower than the mesopause. Below the turbopause, the propagation of the wave is significantly dissipated, while above that, the propagation of the wave is almost free.

The damping of GW activity has also been presented by lidar temperature measurements at mid-latitude sites (Mzé et al., 2014; Rauthe et al., 2008). Both Mzé et al. (2014) and Rauthe et al. (2008) showed that the GW activities presented an annual variation with maximum in winter and minimum in summer, they damped significantly at the upper mesosphere altitudes above ~ 70 km in all seasons, while the damping below ~ 70 km is not so evident. Mzé et al. (2014) observed a nearly undamped propagation of GW in summer in the low mesosphere. Meanwhile, Rauthe et al. (2008) also reported the weakest damping occurring in the summer seasons. Since the effects of GW in the numerical climate and weather prediction models are usually represented simply by parameterization (Kim et al., 2003). there are still large discrepancies between model and measurement results (Geller et al., 2013). Therefore, more attention should be paid to the GW parameterization about these kind of observations in the upper mesosphere and mesopause region to improve the model results.

Seasonal variations of GW activities based on lidar temperature measurements have been investigated at a few low latitude sites (Chane-Ming et al., 2000; Li et al., 2010; Sivakumar et al., 2006). These studies used Rayleigh lidar data and focused mainly on the upper stratosphere and lower mesosphere in an altitude region from 30 to 80 km. They showed the SAO dominated the seasonal variability of GW activities with maxima in both winter and summer and minima near the equinox. Li et al. (2010) related this to the dominated SAO in the mean zonal wind in the tropical stratosphere and lower mesosphere. Considering the different transition of the mean zonal wind in the range 80-95 km in the tropical region noted above, the seasonal variability of GW activity in the tropical upper mesosphere is expected to be different from either the lower altitudes or the mid- and high-latitude regions.

To our knowledge, the seasonal variability of GW activity retrieved from mesospheric lidar temperature data with high temporal and vertical resolution have never been reported from a tropical location.

Such measurements of atmospheric temperature have been conducted with the K Doppler lidar located at the Arecibo Observatory (18.35°N, 66.75°W), Puerto Rico (Friedman and Chu, 2007; Yue et al., 2013, 2016,). Since December 2003, the Arecibo Observatory K Doppler lidar has operated routinely, producing high-quality temperature data. In this report, we estimate the mean temperature, the squared Brunt-Väisälä frequency, N^2 , and the gravity wave potential energy and their annual variability from the temperature dataset. We find an altitude-to-altitude close relationship between the annual variability of the potential energy in this report and that of the mean zonal winds in the literature. Their implications to the role of gravity wave in the MLT are discussed.

2 Observations

The Arecibo K Doppler lidar probes the potassium D1 line to deduce the potassium density and neutral air temperature simultaneously by employing the three-frequency technique (e.g., Friedman and Chu, 2007; Friedman et al., 2003). The temperature was obtained at 0.45/0.9 km vertical and 10/30 minutes temporal resolution, respectively (Friedman and Chu,

2007), and we unify them into profiles with resolutions of 0.9 km and 30 minutes in vertical and temporal dimensions, respectively. This data processing excludes the perturbations relevant to gravity waves with vertical wavelengths and observed periods less than 1.8 km and 1 hour, respectively. Their exclusion may bias the deduced gravity wave associated potential energy estimations towards mid- and low-frequency gravity waves. The root mean square (RMS) temperature errors is about 2 to 3 K at the peak of the K density layer and increase to about 10 K around 85 and 100 km (Friedman and
 5 Chu, 2007; Yue et al., 2017).

Measurements are made only at night in two periods, one from December 2003 to January 2010, the other from November 2015 to April 2017. Data were available for every calendar month. Across the 11 years of the data collection period, 198
 10 observing nights with a total of 1451 hours of data were available at the time of preparing this report. The number of observation nights/hours varies from 4 nights/27 hours in October, to 32 nights/253 hours in January. On average there are 16.5 nights or 121 hours of observation each month. The statistics for the used temperature observations are plotted in Fig. 1 and the numbers of observational nights and durations are summarized for each month in Table 1. When the data are binned into weekly intervals, they cover 45 weeks of a year. On average there are 3.8 nights or 32.2 hours of observation each week. The gaps are at weeks 7,18, 19, 25, 26, 39 and 42. The distribution of the data is quite even during the year. This allows us to
 15 fit the gravity wave activity annual variability through weekly means of temperature.

3 Calculating Methods

The potential energy density E_p can be estimate from temperature observations and then is chosen as a measure of GW activity. E_p is defined as (see, e.g., Vincent et al., 1997)

$$E_p = \frac{1}{2} \left(\frac{g}{N} \right)^2 \left(\frac{T'}{\bar{T}} \right)^2, \quad (1)$$

20 where

$$N^2 = \frac{g}{\bar{T}} \left(\frac{d\bar{T}}{dz} + \frac{g}{c_p} \right), \quad (2)$$

Here g equals to 9.5 ms^{-2} , is the gravitational acceleration in MLT; N is the Brunt-Väisälä frequency calculated according to Eq. (2); \bar{T} is the mean temperature averaging over altitude; T' is the temperature perturbation; and C_p is the constant-pressure heat capacity, equals to $1004 \text{ JK}^{-1}\text{kg}^{-1}$. In Eq. (1), the calculation of E_p depends on the estimations of N , \bar{T} and T' .
 25 The procedure adopted by Gardner and Liu (2007) is closely followed here for the estimation of T' . It includes 4 steps. Step 1: for each night of observation, data points with photon noise errors larger than 30 K in temperature are discarded. The value of 30 K is set based on the fact that the root mean square errors (RMSE) due to photon noise often reach to about 40-50 K near the edges (~ 80 km on the bottom and ~ 105 km on the top) of the temperature profile. Step 2: the linear trend in time at each altitude in the temperature profile is then subtracted to eliminate the potential biases associated with GWs with

periods longer than about twice the observation period. Step 3: Perturbations exceeding three standard deviations from the nightly mean are discarded from the resulted temperature perturbation series at each altitude to remove occasional outliers. Step 4: the vertical mean is subtracted from each temperature perturbation profile to eliminate the influences of the waves with vertical wave length longer than about twice the profile height range (~ 25 km). The resulted temperature perturbation profiles usually cover the height range 80-105 km. Therefore, the weekly composite nights of temperature, N^2 and the consequential E_p usually cover the height range 80-105km. To avoid the uncertainty of the analysis, we focus on the height range 85-100 km where the RMSE of each instantaneous observed temperature usually less than 10 K.

The unified 0.9 km and 30 minutes resolution temperature profiles and the extracted temperature perturbation profiles on each observational night in the same week are binned to the same vertical and temporal grids to construct their composite mean night for each week of a year. The weekly composite night data of \bar{T} is shown in Fig. 2. Temperature Inversion Layers (TILs) can be found in most months.

The weekly composite night data of \bar{T} is first spatially and then temporally smoothed using Hamming windows with full widths at half maximum (FWHM) of 2.7 km and 3 hours, respectively. After that, the weekly composite nights of N^2 and the consequential E_p at 0.9 km and 30 minutes resolutions are estimated through Eq. (2) and (1), respectively. For each parameter, the weekly composite nights are then averaged to derive the weekly mean profiles which are fitted to a harmonic fit model including the annual mean plus 12-month (annual) oscillation and 6-month (semiannual) oscillation. The equation of the model is as following:

$$\Psi(z, t) = \Psi_0(z) + A_{12}(z)\cos\left[\frac{2\pi}{365/7}(t - \varphi_{12}(z))\right] + A_6(z)\cos\left[\frac{4\pi}{365/7}(t - \varphi_6(z))\right] \quad (3)$$

where $\Psi(z, t)$ is the value of a weekly mean parameter at altitude z and week t , expressed in week of the year (1-52), $\Psi_0(z)$ is the annual mean, $A_n(z)$ and $\varphi_n(z)$ ($n = 6, 12$) are the amplitude and phase of the n -month oscillation, respectively.

4 Results

In the following the results of the analysis are shown and discussed with respect to the seasonal variation of the mean temperature (4.1), Square of the Brunt-Väisälä frequency (4.2) and seasonal variation of the gravity wave activity (4.3). Therefore, we plot the fitted seasonal variations of \bar{T} , N^2 , and E_p in Fig. 3a, 4a, and 5a (top left panels), respectively, at 0.9 km vertical and one-week temporal intervals. The amplitudes and phases of the 12-month and 6-month oscillations of the regression model are plotted in Fig. 3c, 4c and 5c (top right panels) and 3d, 4d and 5d (bottom right panels), respectively. In the raw data, temperature error due to photon noise is usually less than 5 K in the altitude range 87-97 km because the K density in this range is usually rather larger (e.g., Yue et al., 2017). To show the seasonal variation of each parameter more clearly, the data between 87 and 97 km are averaged in altitude and then fitted to the same seasonal model consisting of the

annual mean, AO and SAO. Note that it is in a risk of smoothing the temporal variations for those parameters, such as N^2 , which is strongly varying in term of altitude in this range. The averaged results and the fitted curves are plotted in Fig. 3b, 4b and 5b (bottom left panels). The statistical parameters for this fit are summarized in Table 2.

4.1 Seasonal Variation of the Mean Temperature

5 Figure 2 shows the profiles of the weekly mean temperature \bar{T} , the corresponding harmonically fitted temperature is shown in Fig. 3a. It shows that the Arecibo climatology is warmer in late-autumn-early-winter and colder in summer throughout all altitudes. TILs present in most of the time, which are represented by the black cross in Fig. 3a. In spring, TILs occur at ~96 km from late February to April. In summer, TILs appear at ~ 91 km from late May to the first half of September. In winter, TILs occur at ~94 km from the second half of December to the first half of February. The mesopause is above 96 km except
10 in the period from the second half of September to November where it is situated at ~ 96 km.

Figure 3c shows that the amplitudes of the AO are obviously larger than that of the SAO. Fig. 3d shows that the phase (defined as the time of the maximum perturbation) of AO oscillates in a not wide range between day of year (DOY) -60 and 10, while that of SAO varies between DOY 110 and 150. Fig. 3b shows that the mean temperature is warmest between October and November and coldest in July. A secondary peak/trough occurs in April/February.

15 Notice that the warmest temperature occurs around October with shortest observation times which reduce the confidence level of the harmonic fit. However, the observation times in both September and November are longer than 100 hours in more than 10 nights, they help to keep the confidence level of the harmonic fit. Moreover, the temperature structure shown in Fig. 3a agrees well with the temporal variations of the equatorial zonal mean temperature in the range 85-100 km observed by SABER (Xu et al., 2007). The amplitudes and phases of both SAO and AO observed by SABER at 20° N
20 latitude had been shown by Xu et al. (2007) in their middle panels of Figure 10. Comparisons show that the lidar observed phases of both SAO and AO shown in Fig. 3d agree with those obtained by SABER in the same altitude range. The SAO amplitude shown in Fig. 3c agree quite well with that observed by SABER in both magnitude and vertical structure. The lidar AO amplitude show similar vertical structure with that of SABER, but the magnitude of lidar AO amplitude is at least 1 K larger than that observed by SABER. The agreement between lidar and SABER observations gives us more confidence to
25 use the lidar observed temperature data studying the GW activities in latter sections.

Except for the smaller amplitude of SAO oscillation in this study, the phase of SAO, the amplitude and phase of AO of the mean temperature is consistent with a previous study by Friedman and Chu (2007) (see their Fig. 6 to 7), who used data collected between December 2003 and September 2006. Comparing Fig. 3a here to the Fig. 6 in Friedman and Chu (2007), there are some different features in these two climatology results. For example, the temperatures are a bit warmer in the
30 winter months of December and January, but they are obviously colder in the range 90-100 km in March and April in this study. The differences are caused by three reasons. The first and the key point is the lack of adding the smoothed residual temperature back to $T(z, t)$ estimated by using (3) in this study. The second reason is the much more extensive data set from

year 2003 to 2017 covering a whole solar period here. The last reason is the harmonic fit model is in term of week here, while it was in term of month in Friedan and Chu (2007).

4.2 Square of the Brunt-Väisälä frequency

The square of the Brunt-Väisälä frequency N^2 is a good indicator to characterize the atmospheric static stability. Gardner and Liu (2007) indicated that the resulting N^2 were usually overestimated in this way due to the eliminations of gravity waves when the weekly mean temperature profiles were derived by employing data averaging. However, they pointed out that the lower- value regions of N^2 represented well the lower stability of the atmosphere, i.e., the greater wave dissipations. Figure 4a shows that the atmosphere is statically stable on average throughout the height range from 85 to 100 km. The region of greater average stability lay just at and below the temperature inversion layers (shown in Fig. 3a) or just above the mesopause where the mean temperatures increase with increasing altitude.

The fitted curve of $\overline{N^2}$ (average of N^2 between 87 and 97 km height) as shown in Fig. 4b clearly exhibits seasonal variations. The maximum occurs in July and the minimum between October and November, while a secondary maximum occurs between January and February and a secondary minimum in May.

Figure 4c shows that the amplitudes of the 12-month and the 6-month oscillations are comparable throughout most of the altitude range of interest. we allow negative amplitudes to make the phase oscillation of the two components look in order as shown in Fig. 4d. There are several turning points at altitudes ~ 87 km, ~ 92 km, ~ 94 km, ~ 96 km in the profiles of AO and SAO phases. The last three of these altitudes correspond to the altitudes of TILs. This agrees with the fact that the TILs locate at different altitude and N^2 becomes large just below TIL (increased dynamical stability).

4.3 Seasonal Variation of the Gravity Wave Activity

GW activity is directly manifested by the wave energy. Figure 5a shows the contour plots of the harmonic fitted GW potential energy climatology from lidar observation. E_p is coloured in a logarithmic scale (\log_{10}). It can be seen that, below 97 km altitude, E_p always reaches the maximum in equinox seasons, and mostly near spring equinox. More interesting, in equinox seasons the potential energy decreases with altitude from the bottom to ~ 91 km and then shifts to increase with altitude in the range from 91 to 95 km. However, the potential energy is quite smaller in the altitude range 85-95 km during solstices. The energies are low near 91 km throughout all the year. Above 91 km and below an obvious semiannual oscillation is visible at all altitudes in Fig. 5a. The oscillations of potential energy become very weak around 97 km.

Figure 5c shows that the amplitudes of both the 12-month and the 6-month oscillations are comparable at most altitudes The amplitude of 6-month oscillation becomes smaller in the altitude range 94-98 km. The SAO amplitude decreases to almost 0 $\text{J} \cdot \text{kg}^{-1}$ at 97-98 km. Fig. 5d shows the phase of 6-month oscillation is almost independent of altitude. It is quite close to DOY 100 at most altitude. The AO has almost the same phase as the SAO from 88 to 96 km altitude. Its phase shifts to the end of the year near the top edge where it is the dominant seasonal variation. The RMSE of the AO/SAO phase becomes

oddly large near 87/97 km altitudes, respectively, where the AO/SAO amplitude reaches. 0 J.kg^{-1} . It can be seen in Fig. 5a that the seasonal variations of E_p are flat at these two altitudes.

As the seasonal variations of E_p show semi-annual oscillation dominated features with the approximated phases in the altitude range 87-97 km, the mean E_p in the range 87-97 km and the corresponding harmonic fit shown in Fig. 5b represents the behaviour of E_p well. The harmonic fit curve of E_p shows a combination of annual and semi-annual oscillations with the maximum of 404 J.kg^{-1} near vernal equinox and the minimum of 264 J.kg^{-1} in the end of November. The maximum is a factor of 1.5 larger than the minimum.

5 Discussion

5.1 Mesospheric Temperature Inversion Layer

10 We have noticed that obvious TILs occur at ~ 96 km in spring, at ~ 91 km in summer and early autumn, and at ~ 94 km in winter. The TILs in the upper mesosphere over Arecibo had been reported both in case study and/or study of climatology by using subset of the data used in this study (Yue, et al., 2016; Friedman and Chu, 2007). The formation mechanism for TIL in the mesopause region had been reviewed by Meriwether and Gerrard (2004). One primary mechanism for the upper mesosphere TIL is that upward propagating GWs reach a critical level via interaction with the background flow and/or tides. 15 The GW potential energy accumulates with the wave compressed in reaching to the critical level. Xu et al. (2009) analysed satellite observations and showed that the DW1 tide interacted with GW leading to the damping of both DW1 tide and GW, the larger the amplitude of DW1, the larger the damping. Consequently, the occurrence of TIL and the decrease of the GW E_p are expected at and just below the locations where DW1 amplitude is large. Climatology of WACCM Simulations showed that, at 20° N , both the zonal and meridional components of DW1 tide amplitudes are large in height range 80-100 20 km around vernal equinox and in altitude range 90-100 km in summer months from June to August (e.g. Fig. 10 in Smith, 2012). These areas with large DW1 tide amplitude in their Fig. 10 match perfectly with the TILs in Fig. 3a.

5.2 Damp of GW Potential Energy

For freely propagating GWs, the potential energy per unit mass (J.kg^{-1}) should increase exponentially with altitude for the conservation of energy. Fig. 5a shows that the potential energy decreases firstly and then turn to increases gradually with altitude below ~ 97 km in all seasons. Above ~ 97 km, the GW potential energy enhanced significantly with altitude. The solid curve decreases below ~ 92 km and turn to increases above. The increase become significant above 97 km altitude. 25 This behaviour of mean potential energy is much similar to that retrieved from satellite temperature data (Offermann et al., 2006, see their Figures 10 and 11). The altitude of ~ 97 km is in the vicinity of their ‘wave-turbopause’ altitude range, and close to the mesopause over this site [Friedman and Chu, 2007; Yue et al., 2017]. This result indicates that the GW damps

significantly dissipating or depositing energy below about the mesopause (or the wave-turbopause defined by Offermann et al. 2006), but it propagates upward almost freely after penetrating to the thermosphere.

To learn in depth the dissipation of GW in the mesopause region at Arecibo, we multiplied the harmonic fitted E_p with the air density taken from the CIRA-86 reference atmosphere [Fleming et al., 1990], and average every 13 weekly profiles (period of a season) centring at each equinox or solstice. The resulted profiles of the potential energy per unit volume (in $\text{J} \cdot \text{m}^{-3}$) in four seasons are plotted in Fig. 6. If GWs propagate upward without energy dissipation, the lines of energy per unit volume would be vertical. Therefore, the overall left-sloping lines in Fig. 6 indicate that the damp of GW potential energy occur below ~ 97 km in all seasons. The damp of GW potential energy in the mesosphere had been reported by lidar observations at other latitude stations (e. g. Mz  et al., 2014; Rauthe et al., 2008). Both observations of Mz  et al. (2014) and Rauthe et al. (2008) indicate dissipation of GW E_p throughout the mesosphere in all seasons.

The damp of GW E_p in the mesopause region is assumed to be caused by the interaction between DW1 tide and GW (Xu et al. 2009), the larger the amplitude of tide, the larger the energy damp. The climatology of the DW1 tide amplitude at 20°N was shown in Fig. 10 of Smith (2012), which showed the DW1 tidal amplitudes in winter were significantly smaller than the other three seasons, this matches with the smallest damp of GW E_p in winter as shown in Fig. 6 here. The damp of GW E_p indicates the deposition of GW energy and momentum into the background atmosphere, which would lead to the increase of background temperature and/or even the occurrence of TIL. This drives us to investigate the relationship between the damp of GW E_p and the temperature structure in depth. We are excited to find that each profile of the GW potential energy per unit volume ((in $\text{J} \cdot \text{m}^{-3}$) as shown in Fig. 6 shows a rapider damp of energy at and below the TIL altitude of the corresponding season and turns to a much slower damp and/or even conservation of energy above. For examples, the behaviours of the green curve (profile for winter) around 94 km altitude (the altitude of TILs in winter), the blue curve (profile for summer) around 91 km altitude (the altitude of TILs in summer). The black curve (profile for spring) around 96 km altitude (the altitude of TILs in spring). These close connections of the mesospheric TILs with the damp of GW potential energy provide strong support to the mechanism that the upper mesosphere TIL formed due to the interaction of GW with the upper mesospheric wind/diurnal tides through critical level effects.

We notice that in the altitude range 85-95 km, where the GW potential energy damps significantly in all seasons, the background temperature decreases in an oscillational way from ~ 195 K to ~ 185 K. The corresponding mean temperature decreasing rate is of ~ 1 K/km which is extremely smaller than the lapse rate of ~ 9.5 K/km in this altitude region. Above 97 km, the GW potential energy per unit volume either conserves with altitude in summer and winter or turn to increase with altitude in spring as shown in Fig.6. Correspondingly, the background temperatures in Fig. 3a decrease sharper in seasons spring, summer and winter. It is worth to note that in autumn the GW potential energy per unit volume turn to increase at ~ 96 km altitude where the mesopause occurs as shown in Fig. 3a. These results are very valuable in helping to improve the parameterisation of GW in the mesopause region in global circulation models.

5.3 Seasonal variations of GW Potential Energy

We point out a semi-annual cycle of GW E_p with maximum in spring and minimum in summer and a second maximum in autumn and a second minimum in winter in the altitude range 87-97 km. The maximum of the GW E_p alters to autumn below 87 km and above 97 km altitude. These results agree with the observations at other low-latitude stations. Gavrilov et al. (2003) studied the GW seasonal variations by using Medium-Frequency (MF) radar observation over Hawaii (22° N, 160° W). They found a semiannual variation of GW with the maximum intensity at the equinoxes above 83 km, the mean zonal wind had also a mainly semiannual variation in this altitude range. The seasonal variations of GW activities at low-latitude stations are different to those obtained from lidar observations at other latitude stations in the upper mesosphere (Mzé et al., 2014; Rauthe et al., 2006, 2008). Rauthe et al. (2008) provided the seasonal variations of GW E_p at a station of 54° N latitude by using a 6-years of lidar temperature observations from 1 to 105 km. They showed an annual-dominated variation of GW E_p with the maximum in winter and the minimum in summer in the mesopause region. Mzé et al. (2014) reported a semi-annual variation of GW E_p with maxima in winter and in summer and minima during the equinoxes in the upper mesosphere (~75.5 km) by using Rayleigh lidar observations from 1996 to 2012 at a mid-latitude station (~44° N). They showed that the maximum of E_p was about 144 J·kg⁻¹ on average at 75.5 km in August while the minimum of E_p is about a factor of 2.5 smaller than the maximum. The factor of ratio between the maximum and the minimum is obviously larger than that of 1.5 in the altitude range 87-97 km at Arecibo.

The cause of the observed seasonal variations of GW activities in the mesosphere was discussed by several authors. One that is often concerned is the influence of critical level filtering of GW by the background wind (Lindzen, 1981, Yue et al., 2005). The semiannual variation of GW intensity and mean zonal winds reported by Gavrilov et al. (2003) had been attributed to the dependence of GW generation and propagation on background wind and temperature by numerical simulations. In a mid-latitude station Juliusruh (55° N, 13° E), Hoffmann et al. (2010) reported a semiannual variations of GW activity in the upper mesosphere and lower thermosphere with maxima in winter and summer and minima during equinoxes by using MF radar measured winds. This seasonal dependence is assumed to be mainly due to the filtering of GW by the background wind in the stratosphere and lower mesosphere. It is not always the case. Rauthe et al. (2008) did not find a direct correlation between the strength of the GW activity and the background wind direction and/or wind speed taken from European Centre for Medium-Range Weather Forecasts analysis.

Here we also want to check the relation between our observed GW activity and the wind direction and/or wind speed. Some scientific literatures reported studies about seasonal variation of mean zonal wind in the tropical mesopause region (see e.g., Fig. 3 in Garcia et al. 1997; Fig. 3 in Smith 2012). The monthly mean HRDI equatorial zonal wind showed that, the easterly winds were prevailing in equinoxes seasons near 80 km altitude. They then decreased with altitude from 80 km above and turned to increase above ~ 92 km, while the westerly winds prevailed in in the range 80-94 km in solstice seasons, they then turn to be easterly. the reversal is at about 95 km (Smith, 2012). This provides us the opportunity to compare our GW E_p

climatology shown in Fig. 5a with the mean zonal winds climatology shown in the upper panel of the Fig.3 in Smith (2012) season to season and altitude to altitude. Here we focus on the altitude range 85-100 km.

5 Firstly, the mean zonal winds have a dominated semiannual oscillation with westerly winds prevailing in solstice seasons and easterly winds prevailing in equinoxes seasons, meanwhile, our GW E_p has a semiannual oscillation with minima in winter and summer and with maxima during equinoxes. Secondly, the easterly winds are much larger in the altitude range 85-95 km around vernal equinox than around autumn equinox, which corresponds to the fact that the magnitude of GW E_p in spring is significantly greater than that in autumn. This correlation is also verified by the fitted curve in Fig. 5b. The maximum of E_p at vernal equinox with a value of $404 \text{ J} \cdot \text{kg}^{-1}$ is a factor of 1.3 larger than the second maximum of $319 \text{ J} \cdot \text{kg}^{-1}$ at autumn equinox. Thirdly, the largest westerly winds near 90 km in June matches perfectly with the minimum E_p at almost the same altitude and at almost the same time. Fourthly, the zero-wind line near 96 km altitude throughout a whole year is accordance to the almost equal E_p at almost the same altitude in all seasons. Fifthly, the transition of mean zonal winds to easterly winds above 96 km throughout the whole year corresponds well with the overall increase of E_p in the same altitude range. These five features provide strong evidence to an indeed pronounced correlation between the local mean zonal wind field and the lidar observed GW E_p . This correlation agrees perfectly with the connection of wind and GW in the middle atmosphere demonstrated by Lindzen (1981). Correlation between GW potential energy and local winds has been suggested by Wright et al. (2016) in their multi-instrument GW measurements over Tierra del Fuego (54°S , 68°W), which was devoted to the Doppler shifting of waves into the observational filters of the instruments by these winds.

6 Summary and Conclusion

20 The first complete range-resolved climatology of potential energy in the tropical mesopause region is present using 11 years long nocturnal temperature measurements by the K Doppler lidar over the Arecibo Observatory. The mean temperature \bar{T} , the square of the Brunt-Väisälä frequency N^2 and the potential energy of perturbations associated with gravity waves are estimated with high accuracy and resolution from the temperature data. The main characteristics of the observations are as follows.

1. Mesospheric TILs occur in the altitude range 90-95 km in most months except October and November. The decrease rate of background temperature in altitude range 85-95 km is extremely smaller than the lapse rate.
2. The GW potential energy per unit volume (in $\text{J} \cdot \text{m}^{-3}$) damps in the altitude range 85-97 km in all seasons. Close relationship exists between the damp of GW potential energy and the TILs. This provides strong support to the mechanism of the TIL formation in the mesopause region.
3. The seasonal variations of GW potential energy are dominated by the combination of annual and semiannual oscillations at most altitudes. The maxima occur in spring and autumn and the minima occur during solstices. The observed GW potential energy is compared to the wind field as published by Garcia et al. (1997) and Smith (2002), There is indeed a

pronounced altitudinal and temporal correlation between them. This suggests that the seasonal variation of GW activity should be determined mainly by the local wind field through the influence of critical level filtering of GW by the background wind.

5

Competing interests. The authors declare that they have no conflict of interest.

Acknowledgments. The study is supported by NSFC grants 41474128, 61771352 and NSF grant AGS-1744033. The Arecibo Observatory is operated by The University of Central Florida under a cooperative agreement with the National Science Foundation (AST-1744119) and in alliance with Yang Enterprises and Ana G. Méndez -Universidad Metropolitana. The authors thank Dr. John Anthony Smith, Dr. Frank Djuth, Dr. Dave Hysell, Dr. Min-Chang Lee and Eframir Franco Diaz for their help with the observations. In addition, we are grateful to the two anonymous reviewers and Editor Robert Hibbins to improve the paper with their helpful comments.

15 **References**

- Baumgarten, G., Fiedler, J., Hildebrand, J., and Lübken, F.-J.: Inertia gravity wave in the stratosphere and mesosphere observed by Doppler wind and temperature lidar, *Geophys. Res. Lett.*, 42, 10929–10936, <https://doi.org/10.1002/2015GL066991>, 2015.
- Baumgarten, K., Gerding, M., and Lübken, F.-J.: Seasonal variation of gravity wave parameters using different filter methods with daylight lidar measurements at midlatitudes, *J. Geophys. Res.-Atmos.*, 122, 2683–2695, <https://doi.org/10.1002/2016JD025916>, 2017.
- Baumgarten, K., Gerding, M., Baumgarten, G., and Lübken, F.-J.: Temporal variability of tidal and gravity waves during a record long 10-day continuous lidar sounding, *Atmos. Chem. Phys.*, 18, 371–384, <https://doi.org/10.5194/acp-18-371-2018>, 2018.
- 25 Cai, X., Yuan, T., Zhao, Y., Pautet, P. D., Taylor, M. J., and Pendleton, Jr W. R.: A coordinated investigation of the gravity wave breaking and the associated dynamical instability by a Na lidar and an Advanced Mesosphere Temperature Mapper over Logan, UT (41.7°N, 111.8°W), *J. Geophys. Res.-Space*, 119, 6852–6864, <https://doi.org/10.1002/2014JA020131>, 2014.
- Chane-Ming, F., Molinaro, F., Leveau, J., Keckhut, P., and Hauchecorne A.: Analysis of gravity waves in the tropical middle atmosphere over La Reunion Island (21°S, 55°E) with lidar using wavelet techniques, *Ann. Geophys.*, 18, 485–498, <https://doi.org/10.1007/s00585-000-0485-0>, 2000.
- 30 Dunkerton, T. J.: Theory of the Mesopause Semiannual Oscillation, *J. of Atmos. Sci.*, 39, 2681–2690, 1982.

- Fritts, D. C., and Alexander, M. J.: Gravity wave dynamics and effects in the middle atmosphere, *Rev. Geophys.*, 41, 1003, <https://doi.org/10.1029/2001RG000106>, 2003.
- Fleming, E. L., Chandra, S., Barnett, J. J., and Corney, M.: Zonal mean temperature, pressure, zonal wind, and geopotential height as functions of latitude, COSPAR international reference atmosphere: 1986, Part II: Middle atmosphere models, *Adv. Space Res.*, 10, 11–59, [https://doi.org/10.1016/0273-1177\(90\)90386-E](https://doi.org/10.1016/0273-1177(90)90386-E), 1990.
- 5 Friedman, J. S., Tepley, C. A., Raizada, S., Zhou, Q. H., Hedin, J., and Delgado, R.: Potassium Doppler-resonance lidar for the study of the mesosphere and lower thermosphere at the Arecibo Observatory, *J. Atmos. Solar-Terr. Phys.*, 65, 1411-1424, 2003.
- Friedman, J. S., and Chu, X.: Nocturnal temperature structure in the mesopause region over the Arecibo Observatory (18.35°N, 66.75°W): Seasonal variations, *J. Geophys. Res.-Atmos.*, 112, D14107, <https://doi.org/10.1029/2006JD008220>, 10 2007.
- Garcia, R. R., Dunkerton, T. J., Lieberman, R. S., and Vincent, R. A.: Climatology of the semiannual oscillation of the tropical middle atmosphere, *J. Geophys. Res.-Atmos.*, 102, 26019-26032, <https://doi.org/10.1029/97JD00207>, 1997.
- Gardner, C. S., and Liu, A. Z.: Seasonal variations of the vertical fluxes of heat and horizontal momentum in the mesopause 15 region at Starfire Optical Range, New Mexico, *J. Geophys. Res.-Atmos.*, 112, D09113, <https://doi.org/10.1029/2005JD006179>, 2007.
- Gardner, C. S., and Liu, A. Z.: Wave-induced transport of atmospheric constituents and its effect on the mesospheric Na layer, *J. Geophys. Res.-Atmos.*, 115, D20302, <https://doi.org/10.1029/2010JD014140>, 2010.
- Gavrilov, N. M., Riggins, D. M. and Fritts, D. C.: Medium-frequency radar studies of gravity-wave seasonal variations over 20 Hawaii (22°N, 160°W), *J. Geophys. Res.*, 108(D20), 4655, <https://doi.org/10.1029/2002JD003131>, 2003.
- Geller, M., Alexander, M. J., Love, P. T., Bacmeister, J., Ern, M., Hertzog, A., Manzini, E., Preusse, P., Scaife, A., and Zhou, T.: A comparison between gravity wave momentum fluxes in observations and climate models, *J. Clim.*, 26, 6383–6405, <https://doi.org/10.1175/JCLI-D-12-00545.1>, 2013.
- Hirota, I.: Observational evidence of the semiannual oscillation in the tropical middle atmosphere – A review, *Pure Appl. Geophys.*, 118, 217–238, <https://doi.org/10.1007/BF01586452>, 1980.
- 25 Kim, Y. -J., Eckermann, S. D., Chun, H. -Y.: An overview of the past, present and future of gravity-wave drag parameterization for numerical climate and weather prediction models. *Atmosphere-Ocean*, 41, 65-98, <https://doi.org/10.3137/ao.410105>, 2003.
- Li, T., Leblanc, T., McDermid, I. S., Wu, D. L., Dou, X., and Wang, S.: Seasonal and interannual variability of gravity wave 30 activity revealed by long-term lidar observations over Mauna Loa Observatory, Hawaii, *J. Geophys. Res.-Atmos.*, 115, D13103, <https://doi.org/10.1029/2009JD013586>, 2010.
- Lieberman, R. S., Burrage, M. D., Gell, D. A., Hays, P. B., Marshall, A. R., Ortland, D. A., ... Franke, S. J.: Zonal mean winds in the equatorial mesosphere and lower thermosphere observed by the High Resolution Doppler Imager, *Geophys. Res. Lett.*, 20, 2849-2852, <https://doi.org/10.1029/93GL03120>, 1993.

- Lindzen, R. S.: Turbulence and stress owing to gravity wave and tidal breakdown, *J. Geophys. Res.*, 86, 9707-9714, <https://doi.org/10.1029/JC086iC10p09707>, 1981.
- Lu, X., Liu, A. Z., Swenson, G. R., Li, T., Leblanc, T., and McDermid, I. S.: Gravity wave propagation and dissipation from the stratosphere to the lower thermosphere, *J. Geophys. Res.-Atmos.*, 114, D11101, <https://doi.org/10.1029/2008JD010112>,
5 2009.
- Meriwether, J., and J Gerrard, A. J. J.: (2004). Mesosphere inversion layers and stratosphere temperature enhancements. *Rev. Geophys.* 42, <https://doi.org/10.1029/2003RG000133>, 2004.
- Mzé, N., Hauchecorne, A., Keckhut, P., and Thétis, M.: Vertical distribution of gravity wave potential energy from long-term Rayleigh lidar data at a northern middle-latitude site, *J. Geophys. Res.-Atmos.*, 119, 12,069–12,083,
10 <https://doi.org/10.1002/2014JD022035>, 2014.
- Offermann, D., Jarisch, M., Oberheide, J., Gusev, O., Wohltmann, I., Russell III, J. M., and Mlynczak, M. G.: Global wave activity from upper stratosphere to lower thermosphere: A new turbopause concept, *J. Atmos. Solar-Terr. Phys.*, 68, 1709–1729, <https://doi.org/10.1016/j.jastp.2006.01.013>, 2006.
- Rauthe, M., Gerding, M., and Lübken, F.-J.: Seasonal changes in gravity wave activity measured by lidars at mid-latitudes,
15 *Atmos. Chem. Phys.*, 8, 6775-6787, <https://doi.org/10.5194/acp-8-6775-2008>, 2008.
- Sivakumar, V., Rao, P. B., and Bencherif, H.: Lidar observations of middle atmospheric gravity wave activity over a low-latitude site (Gadanki, 13.5°N, 79.2°E), *Ann. Geophys.*, 24, 823–834, <https://doi.org/10.5194/angeo-24-823-2006>, 2006.
- Smith, A.: Global Dynamics of the MLT, *Surv. Geophys.*, 33, 1177-1230, <https://doi.org/10.1007/s10712-012-9196-9> 2012.
- Tsuda, T., Nishida, M., Roeken, C., and Ware, R. H.: A global morphology of gravity wave activity in the stratosphere
20 revealed by the GPS occultation data (GPS/MET), *J. Geophys. Res.-Atmos.*, 105, 7257-7273, <https://doi.org/10.1029/1999JD901005>, 2000.
- Vincent, R. A., Allen, S. J., and Eckermann, S. D.: Gravity Wave Processes: Their Parameterization in Climate Models, NATO ASI Series, Gravity wave parameters in the lower stratosphere, K. Hamilton, 150, Springer, 7–25, 1997.
- Wright, C. J., Hindley, N. P., Moss, A. C., and Mitchell, N. J.: Multi-instrument gravity-wave measurements over Tierra del
25 Fuego and the Drake Passage – Part 1: Potential energies and vertical wavelengths from AIRS, COSMIC, HIRDLS, MLS-Aura, SAAMER, SABER and radiosondes, *Atmos. Meas. Tech.*, 9, 877–908, <https://doi.org/10.5194/amt-9-877-2016>, 2016.
- Xu, J., Smith, A. K., Yuan, W., Liu, H.-L., Wu, Q., Mlynczak, M. G., and Russell III, J. M.: Global structure and long-term variations of zonal mean temperature observed by TIMED/SABER, *J. Geophys. Res.*, 112, D24106, <https://doi.org/10.1029/2007JD008546>, 2007.
- 30 Xu, J., Smith, A. K., Liu, H.-L., Yuan, W., Wu, Q., Jiang, G., Mlynczak, M. G., and Russell III, J. M.: Estimation of the equivalent Rayleigh friction in mesosphere/lower thermosphere region from the migrating diurnal tides observed by TIMED, *J. Geophys. Res.*, 114, D23103, <https://doi.org/10.1029/2009JD012209>, 2009.

- Yuan, T., Heale, C.J., Snively, J.B., Cai, X., Pautet, P.-D., Fish, C., ... Mitchell, N. J.: Evidence of dispersion and refraction of a spectrally broad gravity wave packet in the mesopause region observed by the Na lidar and Mesospheric Temperature Mapper above Logan, Utah, *J. Geophys. Res.-Atmos.*, 121, 579–594, <https://doi.org/10.1002/2015JD023685>, 2016.
- Yue, X., Zhou, Q., Raizada, S., Tepley, C., and Friedman, J.: Relationship between mesospheric Na and Fe layers from simultaneous and common-volume lidar observations at Arecibo, *J. Geophys. Res.-Atmos.*, 118, 905–916, <https://doi.org/10.1002/jgrd.50148>, 2013.
- Yue, X., Zhou, Q., Yi, F., Friedman, J., Raizada, S., and Tepley, C.: Simultaneous and common-volume lidar observations of K/Na layers and temperature at Arecibo Observatory (18°N, 67°W), *J. Geophys. Res.-Atmos.*, 121, 8038-8054, <https://doi.org/10.1002/2015JD024494>, 2016.
- 10 Yue, X., Friedman, J. S., Wu, X., and Zhou, Q. H.: Structure and seasonal variations of the nocturnal mesospheric K layer at Arecibo, *J. Geophys. Res.-Atmos.*, 122, 7260-7275. <https://doi.org/10.1002/2017JD026541>, 2017.
- Yue, X. and Yi, F. Sci. Propagation of gravity wave packet near critical level, *China Ser. E-Technol. Sci.*, 48, 538. <https://doi.org/10.1360/102005-24>, 2005.

Table 1. Arecibo K lidar temperature data used in this study (Days/Hours) by month.

month	Total D/H^a	2004 D/H	2005 D/H	2006 D/H	2007 D/H	2008 D/H	2009 D/H	2010 D/H	2015 D/H	2016 D/H	2017 D/H
Jan.	21/253	4/27		4/44	2/14	6/34		4/35		7/62	5/43
Feb.	7/101		5/33							4/38	3/31
Mar.	20/135	2/9	10/74		4/30	1/4	3/19				
Apr.	21/149	1/5	14/103	3/16		1/8	2/12				1/8
May	6/45	2/12	2/18	2/10							
Jun.	8/62	3/21	2/16				1/1			3/25	
Jul.	18/112	6/41	1/8	1/9		5/26	5/30				
Aug.	16/112	7/46	4/27	2/11	1/6	2/10				2/14	
Sep.	12/107		6/41	4/36		1/8				3/24	
Oct.	4/27	1/5	3/23								
Nov.	11/152	1/2	5/46	4/31			1/9		4/34	3/33	
Dec.	16/196	1/5	4/30	2/19			6/42	3/27 ^b	3/36	5/39	
Total	198/1451	28/171	56/417	22/163	7/50	16/88	18/113	7/62^c	7/70	27/235	9/82

^a D/H stands for Days/Hours; ^b Observed in 2003; ^c Including the observations in 2003.

Table 2. Parameters of mean temperature, temperature variance, squared Brunt-Väisälä frequency and potential energy averaged between 87 and 97 km.

	Annual	Amplitude		Phase (days)		RMS
	Mean	12-month	6-month	12-month	6-month	Residual- σ
Mean temperature (K)	188.7	3.6	1.8	-34	-57	5.5
$\overline{N^2}$ (10^{-4}s^{-2})	4.37	0.09	0.12	160	22	0.37
Potential Energy (Jkg^{-1})	351.8	55.9	42.1	119	-89	141.6

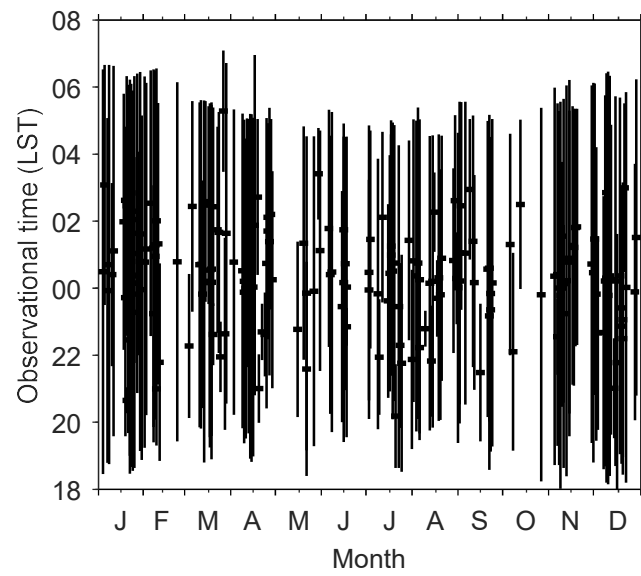


Figure 1: Local time coverage of the used temperature data observed by the K-Doppler lidar at Arecibo from December 2003 to January 2010, and from November 2015 to April 2017.

5

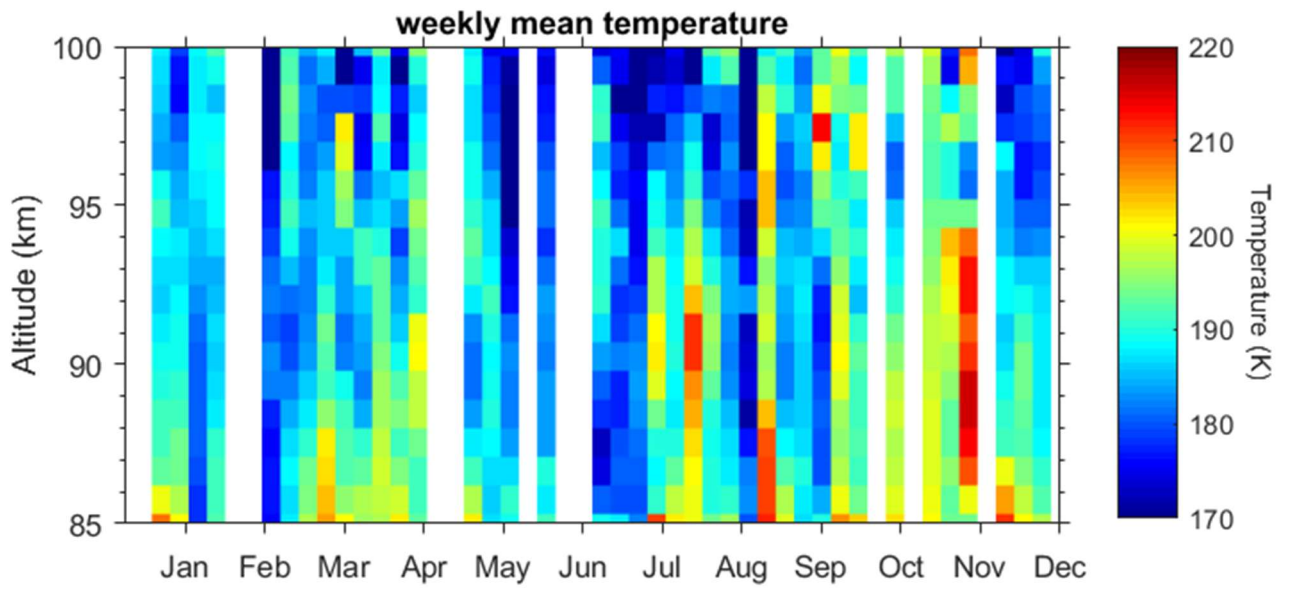
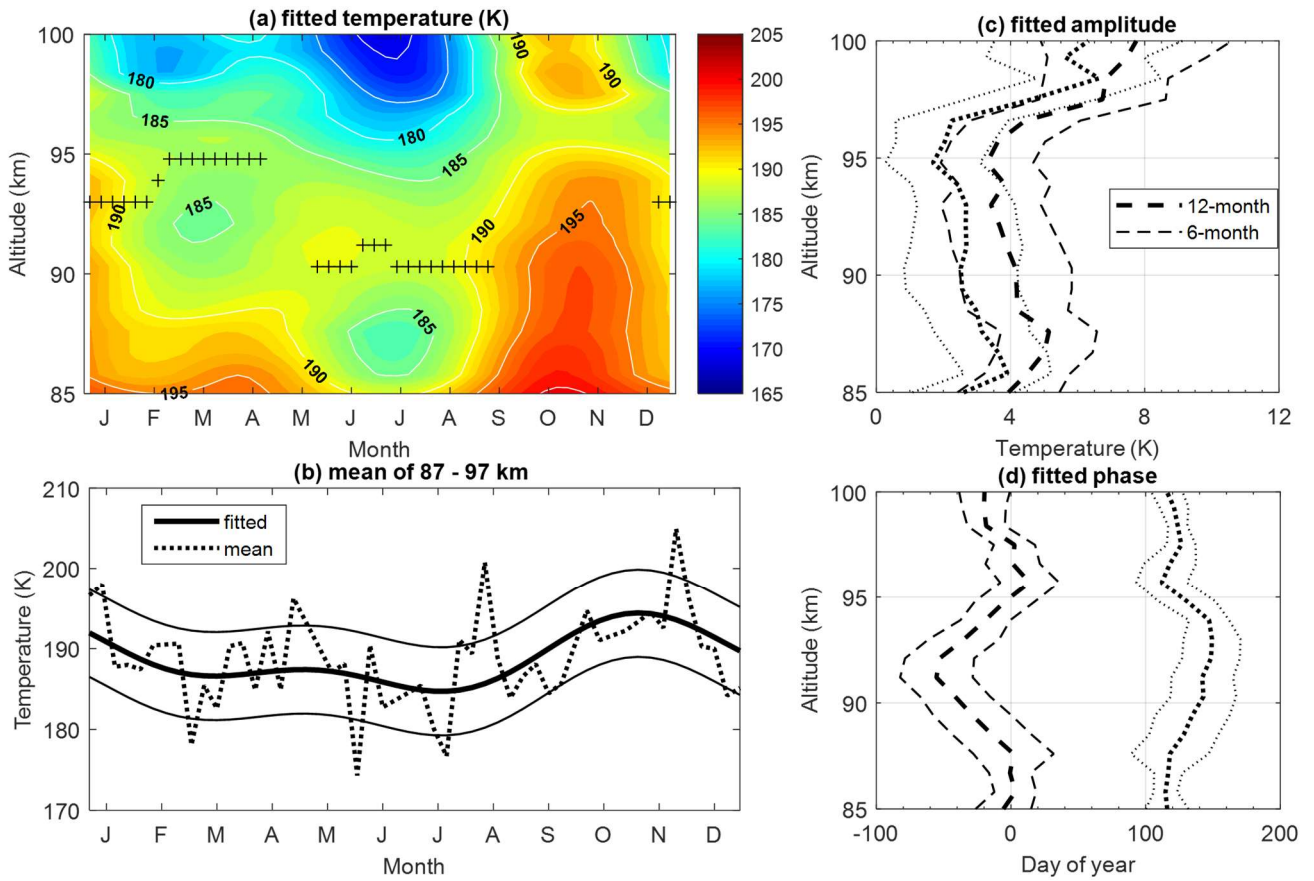


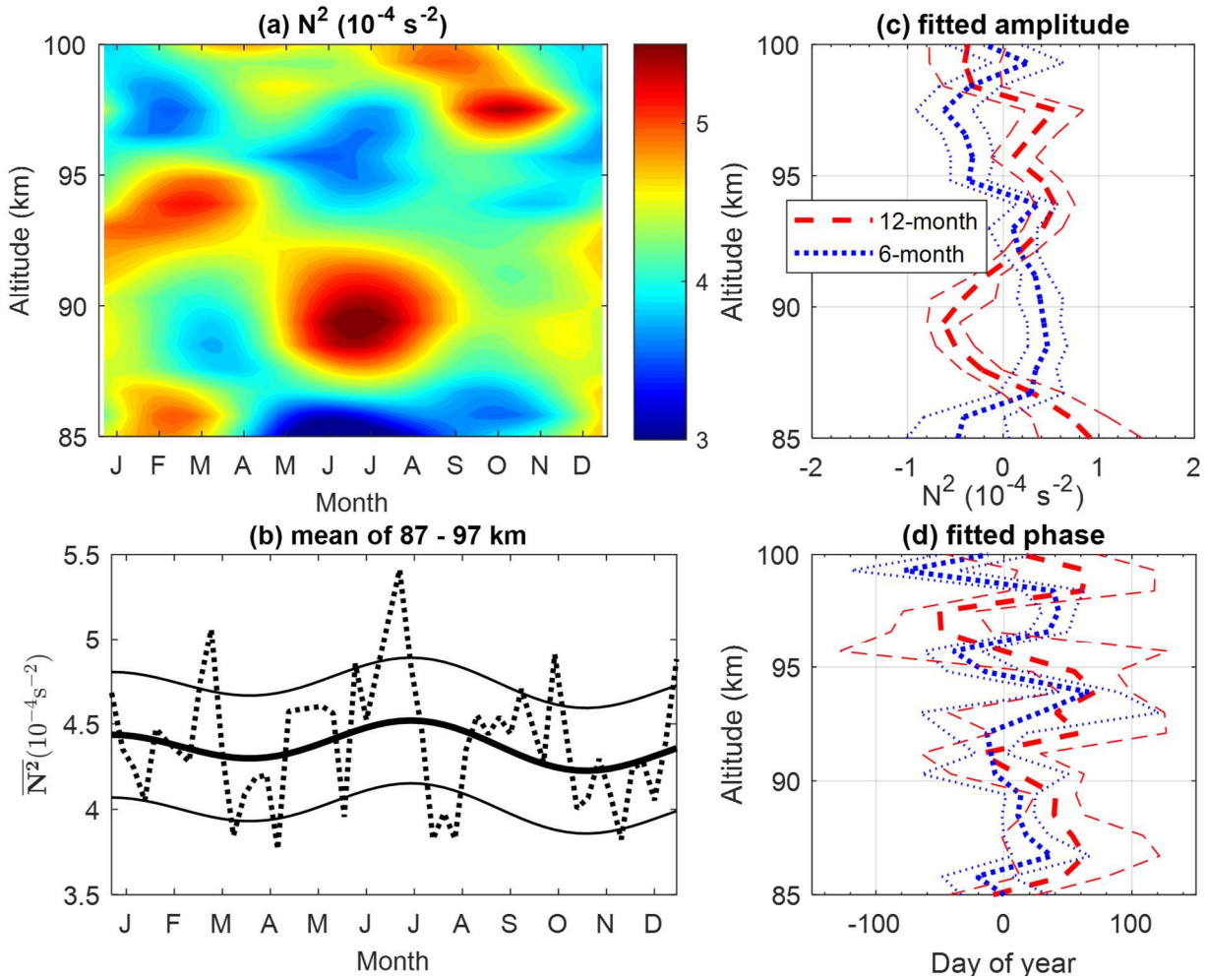
Figure 2: the weekly mean temperature profiles in the mesopause region at Arecibo.

5

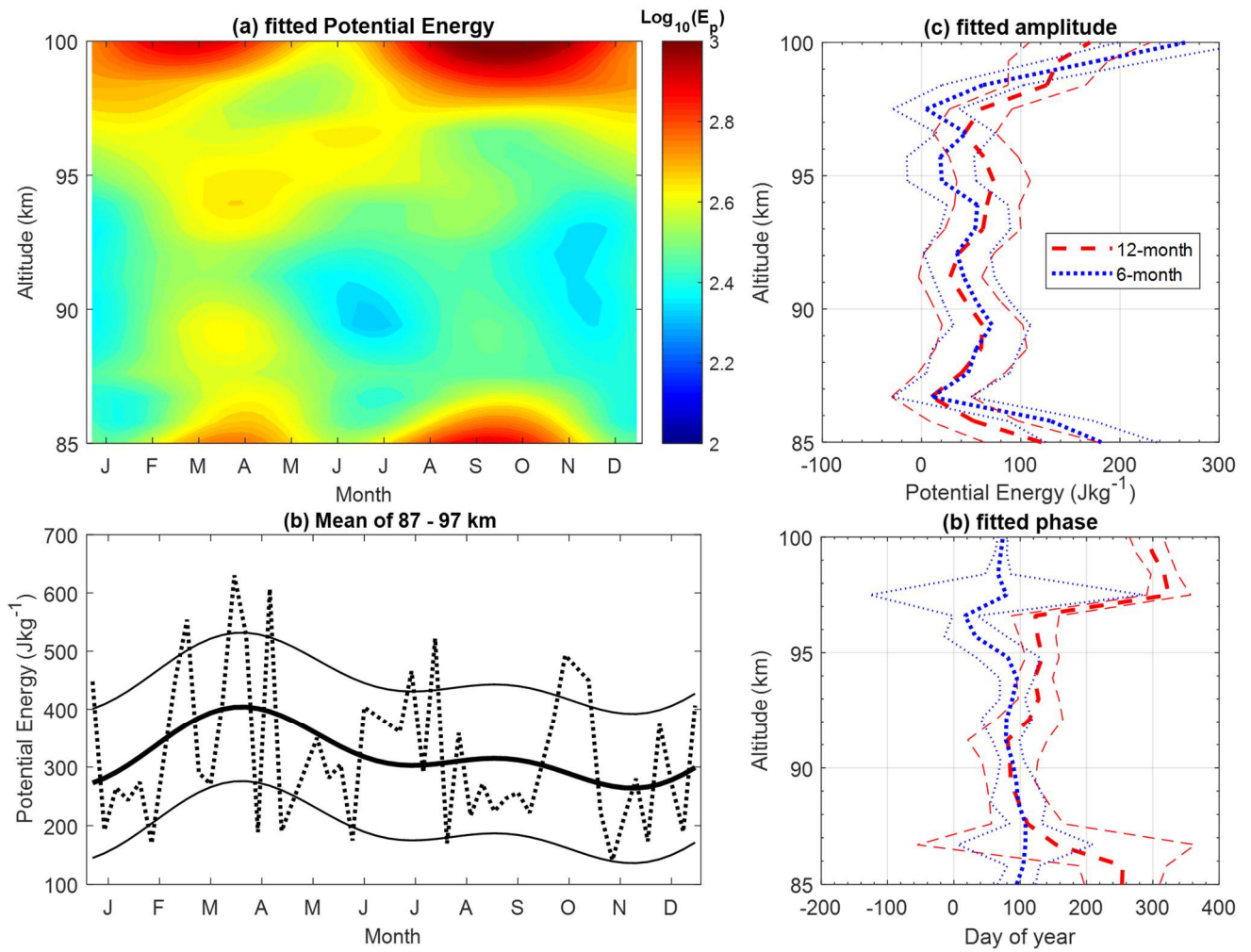


5 Figure 3: (a) Seasonal variations of the harmonic fitted nocturnal temperature plotted versus altitude and month, the crosses represent the altitude of temperature inversion layer, (b) observed (dotted curve) and harmonic fitted (thick solid curve) mean temperature between 87 and 97 km, the width between the thin solid curves and the thick solid curve is 1 standard error (σ), (c) 12-month (dashed curve) and 6-month (dotted curve) amplitudes and their 1σ deviations (thin lines) (d) 12-month (solid curve) and 6-month (dotted curve) phases and their 1σ deviations (thin lines).

10



5 Figure 4: (a) Seasonal variations of the harmonic fitted squared Brunt-Väisälä frequency N^2 plotted versus altitude and month, (b) observed (dotted curve) and harmonic fitted (thick solid curve) mean N^2 between 87 and 97 km, the width between the thin solid curves and the thick solid curve is 1σ , (c) 12-month (red dashed curve) and 6-month (blue dotted curve) amplitudes and their 1σ deviations (thin lines), (d) 12-month (red dashed curve) and 6-month (blue dotted curve) phases.



5 Figure 5: (a) Seasonal variations of the harmonic fitted potential energies plotted versus altitude and month, (b) observed (dotted curve) and harmonic fitted (thick solid curve) mean potential energy between 87 and 97 km, the width between the thin solid curves and the thick solid curve is 1σ , (c) 12-month (red dashed) and 6-month (blue dotted) amplitudes and their 1σ deviations (thin lines), (d) 12-month (red dashed) and 6-month (blue dotted) phases and their 1σ deviations (thin lines).

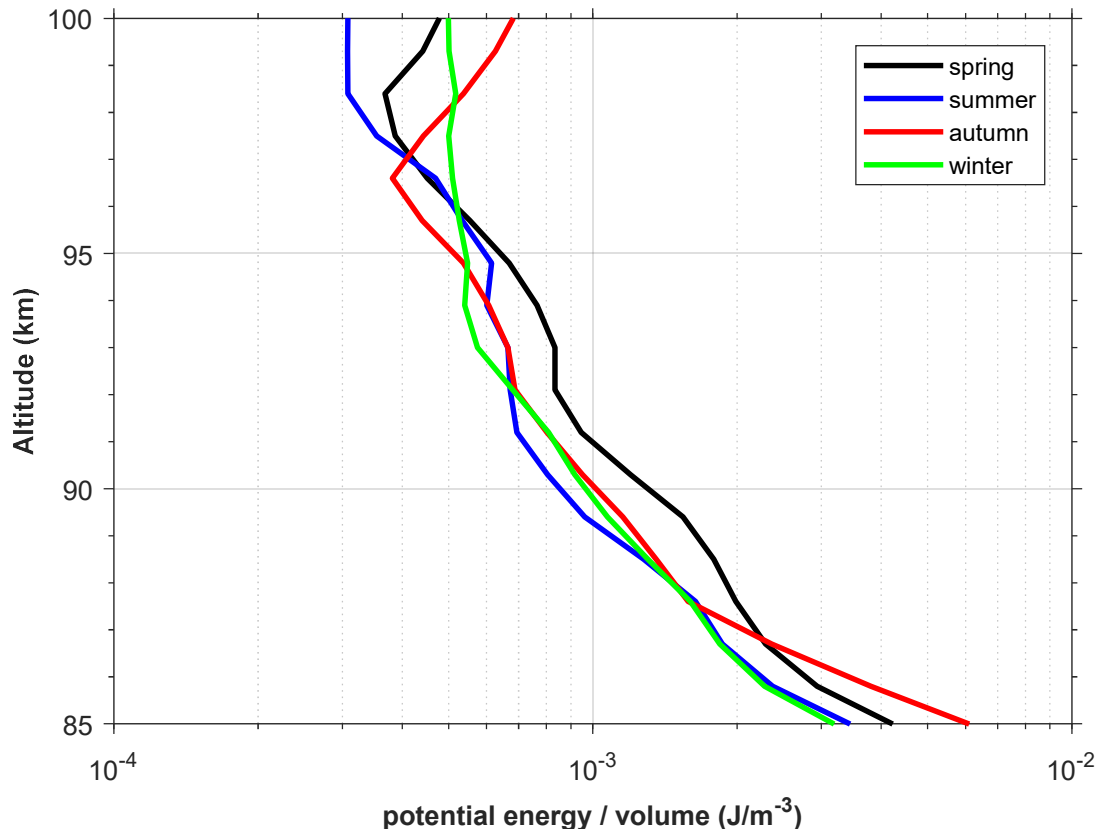


Figure 6: Vertical profiles of the potential energy per unit volume (in $\text{J}\cdot\text{m}^{-3}$) averaged over spring (13 weeks mean centred at vernal equinox, black line), summer (13 weeks mean centred at summer solstice, blue line), autumn (13 weeks mean centred at autumn equinox, red line), winter (13 weeks mean centred at winter solstice, green line).